Investigation on Transformer Inrush Current in Wind Farms Connected MMC-HVDC Systems

Hanwen Wang, Yang Wang, *Senior Member*, *IEEE*, Xianyong Xiao, *Senior Member*, *IEEE*, Zhiquan Ma, and Qunwei Xu

***Abstract*—The transformer inrush current has been a potential threat in wind farms connected modular multilevel converter based high-voltage direct current (WF-MMC-HVDC) system due to the low overcurrent capability of power electronic devices. To investigate this issue, this paper develops a complete harmonic state space (HSS) model of the WF-MMC-HVDC system containing saturable transformers. The severity of the inrush current is investigated under different transformer configurations and the result is compared with EMTP simulations. More importantly, key factors that influence inrush current characteristics in a WF-MMC-HVDC system are studied using the single-input single-output impedance model derived from the linearized HSS model. The results indicate that wind farms have a minor impact on the inrush current characteristics, whereas *V*/*F* controlled modular multilevel converter (MMC) reduces its output voltage during transformer energization, thereby mitigating the severity of the inrush current. The severity of the inrush current largely depends on the resonance point determined by the transmission line. In the case of offshore WF-MMC-HVDC system, long submarine cables may cause severe harmonic amplifications and even do not attenuate for a long time.**

***Index Terms*—Wind farm, modular multilevel converter based high-voltage direct current (MMC-HVDC), transformer inrush current, harmonic state space (HSS), harmonic resonance.**

I. Introduction

MODULAR multilevel converter based high-voltage direct current (MMC-HVDC) has gained great popularity in the last decade due to several distinct advantages, including high power quality, free of commutation failures, etc. [1]. Since 2020, several high-voltage modular multilevel converter (MMC) projects have been completed in China, including Zhangbei and Rudong projects [2], mainly for long-distance power transmission of wind power. As interfacing inverters of wind generators and MMC are both power electronic devices, their overcurrent capabilities are limited and thus suffer from the inrush current induced by the transformer energization, e.g., the inrush current caused the protection trip in Rudong wind farm (WF) connected MMC-HVDC (WF-MMC-HVDC) system [3] in 2021.

Extensive research on inrush current has been documented in the literature for a considerable period, and it remains a ongoing study to the present day. For instance, [4] proposes a transformer inrush current identification method based on the differential current, which can accurately distinguish internal faults from inrush current. References [5] and [6] introduce effective methods for calculating residual flux in transformers. In [7] and [8], strategies to suppress the inrush current are presented based on asynchronous reclosing technology and the grid forming inverter, respectively. Through literature review, it can be found that the recent research mainly focuses on the identification and mitigation of the inrush current, whereas very few of them investigates the characteristics and propagation. Different from the conventional power grid, WF-MMC-HVDC systems involve heterogeneous inverters with different control strategies. The response mechanism of these devices to the inrush current has not been thoroughly investigated, which is the motivation to conduct this research. The findings would facilitate the understanding of the practical incidents and the design of mitigation strategies.

Due to the highly nonlinear nature of transformer energization, time-domain simulation is the most common method to investigate the impact of the inrush current. The method shows high-fidelity, but cannot provide deep insights into the phenomenon, thus providing limited help on the cause identification and mitigation. Besides, a frequency-domain method named dynamic phasor method (DPM) gradually gains its popularity in recent years [9]-[13]. DPM employs time-varying Fourier series to transform a linear time-periodic (LTP) system into a linear time-invariant (LTI) system, which simplifies the calculation of the LTP system and is capable of accurately reflecting the dynamics of harmonics during the transient [9], [10]. DPM has been successfully applied in various scenarios such as thyristor-controlled rectifiers [11], high-voltage direct current (HVDC) transmission systems [12], and microgrids [13].

Similar to DPM, harmonic state space (HSS) is another LTP modeling method that effectively captures the characteristics of LTP systems using coupled harmonic phasors [14].

Manuscript received: June 15, 2024; revised: December 9, 2024; accepted: February 21, 2025. Date of CrossCheck: March 24, 2025. Date of online publication: April 25, 2025.

This work was supported by the Science and Technology Project of State Grid Corporation of China (SGCC) (No. 5500-202319174A-1-1-ZN).

H. Wang, Y. Wang (corresponding author), and X. Xiao are with the College of Electrical Engineering, Sichuan University, Chengdu, China (e-mail: 976898554@qq.com; fwang@scu.edu.cn; xiaoxianyong@163.com).

Z. Ma and Q. Xu are with State Grid Zhejiang Electric Power Research Institute, Zhejiang, China (e-mail: mnzq_wisdomer@163. com; qunwei_xu@163. com).

DOI: 10.35833/MPCE.2024.000628

Compared with DPM, the HSS modeling is more straightforward and easy to use [15]. More importantly, as HSS establishes harmonic phasors in complex domain, the impedance model of the system can be directly obtained through linearization and Laplace transform. Therefore, the method is very suitable for the unified transient and stability analysis. Reference [16] employs HSS to model distribution networks. Both the transient response and the small-signal stability analysis are investigated. Yet, [16] does not investigate the transformer inrush current issue. In [17] and [18], HSS is, for the first time, applied to model Y_g-Y_g transformers and the inrush current when the no-load energization is simulated. In [19], an HSS model of a static synchronous compensator (STATCOM) with a saturable transformer is established, which only explains the modeling process and does not analyze the interaction between the STATCOM and the inrush current. Moreover, systems in the above literature differ significantly from the one considered in this paper. In [16]-[19], a Thevenin equivalent circuit is used to represent the voltage source, whereas a *V*/*F* controlled MMC is considered in this paper. Therefore, it is difficult to conclude the characteristics of the inrush current in WF-MMC-HVDC systems from the previous work.

In view of the above, this paper presents a comprehensive investigation on the transformer inrush current in WF-MMC-HVDC systems. To achieve this goal, the HSS modeling technique is adopted to establish dynamic models of a WF-MMC-HVDC system with saturable transformers. The characteristics of the inrush current can be then investigated using harmonic phasors during the transient, and key influencing factors are revealed using linearized impedance models. The main contributions of this paper are summarized as follows.

1) Detailed HSS models for three commonly-used transformers are developed according to their magnetic and electric circuits, which lay the foundation for the transformer inrush current related research. Based on these models, it is revealed in this paper that Y-Y_g transformers produce smaller inrush currents compared with Y_g-Y and Y_g-D transformers.

2) By establishing the complete HSS model including WF-MMC-HVDC system and saturable transformers, the paper points out that the MMC with *V*/*F* control can alleviate the severity of the inrush current. The reason is analytically explained by the mathematical model of MMCs.

3) Taking advantage of modal analysis, key factors influencing characteristics of harmonic resonances in WF-MMC-HVDC systems are identified. It is found that the capacitance of transmission lines and MMC impedances have significant impact, while the influence of WFs and line inductances are limited. These findings would support the inrush current mitigation at the planning stage.

The remainder of this paper is organized as follows. Sections II establishes WF-MMC-HVDC system model. Sections III presents model validation and inrush current analysis. Section IV investigates the influencing factors. The conclusion is presented in Section V.

II. WF-MMC-HVDC System Model

In this section, a WF-MMC-HVDC system shown in the Supplementary Material A Fig. SA1 [20] is established using the HSS modeling technique [16]-[19]. A 900 MVA MMC employs the *V*/*F* control to form the grid voltage, and the DC side is simplified as a DC voltage source. The capacity of the entire wind power system is 900 MVA, where 700 MVA wind generators are in operation and 200 MVA wind generators are shut down. The WF consists of Type-4 wind generators, where the grid-side converter (GSC) adopts DC voltage control and the machine-side converter (MSC) adopts speed control. The parameters used in the system are presented in Tables I to III and the design method can be found in [20], [21].

TABLE I
No-load Transformer Parameters

Parameter	Value
Transformer capacity	200 MVA
Transformer ratio	230 kV/35 kV
Excitation resistance	10000 Ω
Leakage reactance	0.11 p.u.

TABLE II
WF-MMC-HVDC System Parameters

Component	Parameter	Value
MMC station	DC side voltage	500 kV
	Arm inductance	100 mH
	Rated power	900 MW
	Arm resistance	0.3 Ω
	Submodule number	256
	Module capacitance	8 mF
	Transformer winding connection	Y_g-D
	Proportional parameter and integral parameter of circulating current suppression control (CCSC)	20, 2000
	Proportional parameter and integral parameter of voltage loop	1, 100
	Proportional parameter and integral parameter of current loop	1, 10
	Control delay	250 μs
	System frequency	50 Hz
	Transformer ratio	290 kV/ 230 kV
	Transformer leakage reactance	0.12 p.u.
WF	Filtering inductance	1.11 μH
	Rated power	700 MW
	Rated AC voltage	690 V
	DC voltage	1450 V
	Transformer winding connection	Y-Y_g
	Proportional parameter and integral parameter of DC voltage loop	5, 10
	Proportional parameter and integral parameter of current loop	1.2, 50
	Proportional parameter and integral parameter of phase-locked loop (PLL)	20, 100
	Number of wind turbine	350
	Transformer ratio	230 kV/ 0.69 kV
	Transformer leakage reactance	0.12 p.u.

TABLE III
LINE PARAMETER

Parameter	Value
Unit inductance	0.976 mH/km
Unit capacitance	0.011 uF/km
Unit resistance	0.0626 Ω/km
Length of line A	20 km
Length of line B	20 km

A. HSS Model of Saturable Transformer

Accurate modeling of saturable transformers is the key for the inrush current analysis. In practical WF-MMC-HVDC projects, common transformer winding connections are Y_g-Y, Y_g-D, and Y-Y_g [22]. This subsection establishes the HSS model of a Y_g-D transformer. The detailed HSS models of other two configurations can be found in the Supplementary Material B.

In this paper, a polynomial form is employed to simulate the magnetization current $i_{j\psi}(t)$ as:

$$i_{j\psi}(t)=a_1\psi_j(t)+a_3\psi_j^3(t)+a_5\psi_j^5(t)+\ldots+a_n\psi_j^n(t) \tag{1}$$

where ψ is the magnetic flux acting on the excitation inductance and satisfies $\mathrm{d}\psi/\mathrm{d}t=v$, and v is the excitation branch voltage; a_k $(k=1,3,...,n)$ is the coefficient for each term, and n is an odd number; and subscript j represents one of the three phases. Based on the data provided by the manufacturer, the knee point voltage of the transformer is 1.2 p.u. and the corresponding magnetizing current I_k is set to be 0.5% of the rated current of the transformer. The least square method is used for fitting, resulting in the magnetization characteristic curve of the transformer, as illustrated in Fig. 1.

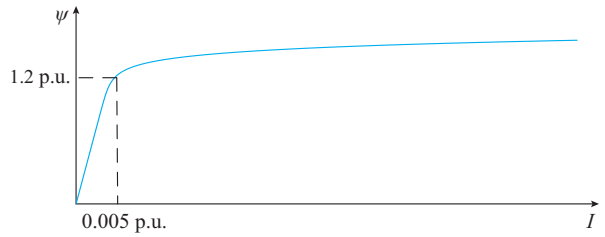

Fig. 1. Magnetization characteristic curve of transformer.

The equivalent circuit of the three-phase Y_g-D transformer is shown in Fig. 2, where L_{j1} and r_{j1} are the total equivalent impedances on the primary side of the transformer; L_{j2} and r_{j2} are the equivalent impedances on the secondary side; i_d is the circulating current on the secondary side; r_{mag} is the magnetizing resistance used to simulate transformer losses; and i_{inrj} is the three-phase inrush current.

Based on Fig. 2 and (1), the corresponding formulation of phase A can be derived based on Kirchhoff's voltage law (KVL) as:

$$\begin{cases} v_A=L_{A1}\dfrac{\mathrm{d}i_{inrA}}{\mathrm{d}t}+r_{A1}i_{inrA}+r_{mag}(i_{inrA}-i_d-i_{A\psi}) \\ v=\dfrac{\mathrm{d}\psi_A}{\mathrm{d}t}=r_{mag}(i_{inrA}-i_d-i_{A\psi}) \\ i_{A\psi}=a_1\psi_A+a_3\psi_A^3+a_5\psi_A^5+\ldots+a_n\psi_A^n \end{cases} \tag{2}$$

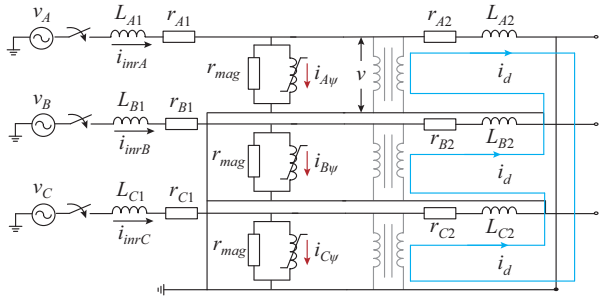

Fig. 2. Equivalent circuit of the three-phase Y_g-D transformer.

By moving the differential terms in (2) to the left side of the equation, (2) can be rewritten as:

$$\begin{cases} \dfrac{\mathrm{d}i_{inrA}}{\mathrm{d}t}=-\dfrac{r_{A1}+r_{mag}}{L_{A1}}i_{inrA}+\dfrac{v_A}{L_{A1}}+\dfrac{r_{mag}}{L_{A1}}i_{A\psi}+\dfrac{r_{mag}}{L_{A1}}i_d \\ \dfrac{\mathrm{d}\psi_A}{\mathrm{d}t}=-r_{mag}(a_1+a_3\psi_A^2+a_5\psi_A^4+\ldots+a_n\psi_A^{n-1})\psi_A+ \\ \qquad r_{mag}i_{inrA}-r_{mag}i_d \end{cases} \tag{3}$$

Then, expanding (3) to three phases as follows:

$$\begin{cases} \dfrac{\mathrm{d}i_{inrA}}{\mathrm{d}t}=-\dfrac{r_{A1}+r_{mag}}{L_{A1}}i_{inrA}+\dfrac{r_{mag}}{L_{A1}}i_{A\psi}+\dfrac{v_A}{L_{A1}}+\dfrac{r_{mag}}{L_{A1}}i_d \\ \dfrac{\mathrm{d}\psi_A}{\mathrm{d}t}=-r_{mag}(a_1+a_3\psi_A^2+a_5\psi_A^4+\ldots+a_n\psi_A^{n-1})\psi_A+ \\ \qquad r_{mag}i_{inrA}-r_{mag}i_d \\ \dfrac{\mathrm{d}i_{inrB}}{\mathrm{d}t}=-\dfrac{r_{B1}+r_{mag}}{L_{B1}}i_{inrB}+\dfrac{r_{mag}}{L_{B1}}i_{B\psi}+\dfrac{v_B}{L_{B1}}+\dfrac{r_{mag}}{L_{B1}}i_d \\ \dfrac{\mathrm{d}\psi_B}{\mathrm{d}t}=-r_{mag}(a_1+a_3\psi_B^2+a_5\psi_B^4+\ldots+a_n\psi_B^{n-1})\psi_B+ \\ \qquad r_{mag}i_{inrB}-r_{mag}i_d \\ \dfrac{\mathrm{d}i_{inrC}}{\mathrm{d}t}=-\dfrac{r_{C1}+r_{mag}}{L_{C1}}i_{inrC}+\dfrac{r_{mag}}{L_{C1}}i_{C\psi}+\dfrac{v_C}{L_{C1}}+\dfrac{r_{mag}}{L_{C1}}i_d \\ \dfrac{\mathrm{d}\psi_C}{\mathrm{d}t}=-r_{mag}(a_1+a_3\psi_C^2+a_5\psi_C^4+\ldots+a_n\psi_C^{n-1})\psi_C+ \\ \qquad r_{mag}i_{inrC}-r_{mag}i_d \end{cases} \tag{4}$$

Similarly, based on KVL and Fig. 3, the voltage equation involving i_d can be identified as:

$$\begin{cases} r_{mag}(i_{inrA}-i_{A\psi}-i_d)=L_{A2}\dfrac{\mathrm{d}i_d}{\mathrm{d}t}+r_{A2}i_d \\ r_{mag}(i_{inrB}-i_{B\psi}-i_d)=L_{B2}\dfrac{\mathrm{d}i_d}{\mathrm{d}t}+r_{B2}i_d \\ r_{mag}(i_{inrC}-i_{C\psi}-i_d)=L_{C2}\dfrac{\mathrm{d}i_d}{\mathrm{d}t}+r_{C2}i_d \end{cases} \tag{5}$$

Generally, the transformer is three-phase balanced. Thus, it is reasonable to assume $r_{A1(2)}=r_{B1(2)}=r_{C1(2)}$, $L_{A1(2)}=L_{B1(2)}=L_{C1(2)}$. Therefore, (5) can be rewritten as:

$$\frac{\mathrm{d}i_d}{\mathrm{d}t}=-\frac{r_{mag}+r_{A2}}{L_{A2}}i_d+\frac{r_{mag}}{3L_{A2}}(i_{inrA}+i_{inrB}+i_{inrC}-i_{A\psi}-i_{B\psi}-i_{C\psi}) \tag{6}$$

Finally, the HSS model of the three-phase Y_g-D transformer can be derived as:

$$\begin{cases} \dfrac{\mathrm{d}\boldsymbol{i}_{inrj}}{\mathrm{d}t} = -\left(\dfrac{r_{j1}+r_{mag}}{L_{j1}}\boldsymbol{EI}+\boldsymbol{N}\right)\boldsymbol{i}_{inrj} + \dfrac{r_{mag}}{L_{j1}}\boldsymbol{i}_{j\psi} + \dfrac{1}{L_{j1}}\boldsymbol{v}_j + \dfrac{r_{mag}}{L_{j1}}\boldsymbol{i}_d \\ \dfrac{\mathrm{d}\boldsymbol{\psi}_j}{\mathrm{d}t} = -[r_{mag}(a_1\boldsymbol{EI}+a_3\boldsymbol{\Gamma}(\boldsymbol{\psi}_j)^2+a_5\boldsymbol{\Gamma}(\boldsymbol{\psi}_j)^4+\ldots+ \\ \qquad a_n\boldsymbol{\Gamma}(\boldsymbol{\psi}_j)^{n-1})+\boldsymbol{N}]\boldsymbol{\psi}_j + r_{mag}\boldsymbol{i}_{inrj} - r_{mag}\boldsymbol{i}_d \\ \dfrac{\mathrm{d}\boldsymbol{i}_d}{\mathrm{d}t} = -\left(\dfrac{r_{mag}+r_{A2}}{L_{A2}}\boldsymbol{EI}+\boldsymbol{N}\right)\boldsymbol{i}_d + \dfrac{r_{mag}}{3L_{A2}}(\boldsymbol{i}_{inrA}+\boldsymbol{i}_{inrB}+\boldsymbol{i}_{inrC}- \\ \qquad \boldsymbol{i}_{A\psi}-\boldsymbol{i}_{B\psi}-\boldsymbol{i}_{C\psi}) \end{cases} \tag{7}$$

where $\boldsymbol{N}=\mathrm{diag}\{-\mathrm{j}h\omega,\ldots,-\mathrm{j}\omega,0,\mathrm{j}\omega,\ldots,\mathrm{j}h\omega\}$; $\boldsymbol{EI}$ is a $n\times n$ identity matrix; $\boldsymbol{\Gamma}$ is the Toeplitz matrix form of the variable; and variables in bold represent the matrix form of those variables.

B. Modeling of WF-MMC-HVDC System

As MMCs and WFs are both power electronic devices that involve hardware and software systems [23], their modeling processes are similar. To avoid the repetition, only the modeling process of MMCs is explained in this paper. MMC model primarily consists of main circuits, *V/F* control loop, and CCSC.

1) Main Circuit

Figure 3 depicts the equivalent circuit for phase *A* of the MMC. u_{dcu} and u_{dcl} are the DC voltages of the positive and negative poles, respectively, each with a value of $1/2u_{dc}$; i_{dc} is the DC side current; i_{uA}, i_{lA} and u_{cumA}, u_{clmA} are the upper and lower arm currents and voltages, respectively; i_{cA} is the circulating current; u_{2A} and i_{2A} are the phase-*A* voltage and current on the AC side, respectively; and R_{arm}, L_{arm}, and C_{arm} are the equivalent arm impedances.

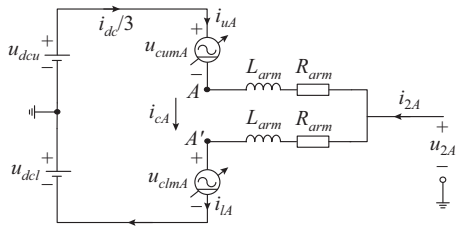

Fig. 3. Equivalent circuit for phase *A* of MMC.

Applying the KVL to the circuit, the equations of phase *A* can be obtained as [24]:

$$\begin{cases} \dfrac{\mathrm{d}i_{cA}}{\mathrm{d}t} = -\dfrac{R_{arm}}{L_{arm}}i_{cA} - \dfrac{n_{uA}}{2L_{arm}}u_{cumA} - \dfrac{n_{lA}}{2L_{arm}}u_{clmA} + \dfrac{u_{dc}}{2L_{arm}} \\ \dfrac{\mathrm{d}i_{2A}}{\mathrm{d}t} = -\dfrac{R_{arm}}{L_{arm}}i_{2A} + \dfrac{n_{uA}}{L_{arm}}u_{cumA} - \dfrac{n_{lA}}{L_{arm}}u_{clmA} + \dfrac{2u_{2A}}{L_{arm}} \\ \dfrac{\mathrm{d}u_{cumA}}{\mathrm{d}t} = \dfrac{N_m n_{uA}}{C_{arm}}i_{cA} - \dfrac{N_m n_{uA}}{2C_{arm}}i_{2A} \\ \dfrac{\mathrm{d}u_{clmA}}{\mathrm{d}t} = \dfrac{N_m n_{lA}}{C_{arm}}i_{cA} + \dfrac{N_m n_{lA}}{2C_{arm}}i_{2A} \end{cases} \tag{8}$$

where n_{uA} and n_{lA} are the modulation signals for the upper and lower arm of phase *A*, respectively; and N_m is the number of submodules.

Based on HSS theory, the three-phase main circuit of the MMC can be formulated in HSS domain as:

$$\begin{cases} \dfrac{\mathrm{d}\boldsymbol{i}_{cj}}{\mathrm{d}t} = \left(-\dfrac{R_{arm}}{L_{arm}}\boldsymbol{EI}-\boldsymbol{N}\right)\boldsymbol{i}_{cj} - \dfrac{\boldsymbol{\Gamma}(n_{uj})}{2L_{arm}}\boldsymbol{u}_{cumj} - \dfrac{\boldsymbol{\Gamma}(n_{lj})}{2L_{arm}}\boldsymbol{u}_{clmj} + \dfrac{\boldsymbol{u}_{dc}}{2L_{arm}} \\ \dfrac{\mathrm{d}\boldsymbol{i}_{2j}}{\mathrm{d}t} = \left(-\dfrac{R_{arm}}{L_{arm}}\boldsymbol{EI}-\boldsymbol{N}\right)\boldsymbol{i}_{2j} + \dfrac{\boldsymbol{\Gamma}(n_{uj})}{L_{arm}}\boldsymbol{u}_{cumj} - \dfrac{\boldsymbol{\Gamma}(n_{lj})}{L_{arm}}\boldsymbol{u}_{clmj} + \dfrac{2\boldsymbol{u}_{2j}}{L_{arm}} \\ \dfrac{\mathrm{d}\boldsymbol{u}_{cumj}}{\mathrm{d}t} = (\boldsymbol{0}\times\boldsymbol{EI}-\boldsymbol{N})\boldsymbol{u}_{cumj} + \dfrac{N_m\boldsymbol{\Gamma}(n_{uj})}{C_{arm}}\boldsymbol{i}_{cj} - \dfrac{N_m\boldsymbol{\Gamma}(n_{uA})}{2C_{arm}}\boldsymbol{i}_{2j} \\ \dfrac{\mathrm{d}\boldsymbol{u}_{clmj}}{\mathrm{d}t} = (\boldsymbol{0}\times\boldsymbol{EI}-\boldsymbol{N})\boldsymbol{u}_{clmj} + \dfrac{N_m\boldsymbol{\Gamma}(n_{lj})}{C_{arm}}\boldsymbol{i}_{cj} + \dfrac{N_m\boldsymbol{\Gamma}(n_{lj})}{2C_{arm}}\boldsymbol{i}_{2j} \end{cases} \tag{9}$$

where the variables in bold represent the matrix form of those variables.

2) V/F Control Loop

MMC converter employs a *V/F* control loop to form the grid voltage, which includes an outer AC voltage control and an inner current control. In HSS domain, the park transformation can be expressed as:

$$\begin{cases} \boldsymbol{u}_{2d} = \boldsymbol{\Gamma}(\cos(\omega_0 t))\boldsymbol{u}_{2A} + \boldsymbol{\Gamma}\left(\cos\left(\omega_0 t - \dfrac{2\pi}{3}\right)\right)\boldsymbol{u}_{2B} + \\ \qquad \boldsymbol{\Gamma}\left(\cos\left(\omega_0 t + \dfrac{2\pi}{3}\right)\right)\boldsymbol{u}_{2C} \\ \boldsymbol{u}_{2q} = -\boldsymbol{\Gamma}(\sin(\omega_0 t))\boldsymbol{u}_{2A} - \boldsymbol{\Gamma}\left(\sin\left(\omega_0 t - \dfrac{2\pi}{3}\right)\right)\boldsymbol{u}_{2B} - \\ \qquad \boldsymbol{\Gamma}\left(\sin\left(\omega_0 t + \dfrac{2\pi}{3}\right)\right)\boldsymbol{u}_{2C} \\ \boldsymbol{i}_{2d} = \boldsymbol{\Gamma}(\cos(\omega_0 t))\boldsymbol{i}_{2A} + \boldsymbol{\Gamma}\left(\cos\left(\omega_0 t - \dfrac{2\pi}{3}\right)\right)\boldsymbol{i}_{2B} + \\ \qquad \boldsymbol{\Gamma}\left(\cos\left(\omega_0 t + \dfrac{2\pi}{3}\right)\right)\boldsymbol{i}_{2C} \\ \boldsymbol{i}_{2q} = -\boldsymbol{\Gamma}(\sin(\omega_0 t))\boldsymbol{i}_{2A} - \boldsymbol{\Gamma}\left(\sin\left(\omega_0 t - \dfrac{2\pi}{3}\right)\right)\boldsymbol{i}_{2B} - \\ \qquad \boldsymbol{\Gamma}\left(\sin\left(\omega_0 t + \dfrac{2\pi}{3}\right)\right)\boldsymbol{i}_{2C} \end{cases} \tag{10}$$

where $\omega_0 = 2\pi f_0$, $f_0 = 50$ Hz; and $\boldsymbol{u}_{2d}$, $\boldsymbol{u}_{2q}$ and $\boldsymbol{i}_{2d}$, $\boldsymbol{i}_{2q}$ are the matrix forms of the *d*- and *q*-axis components of u_{2ABC} and i_{2ABC} at the point of common coupling (PCC) of MMC, respectively. Then, the outer AC voltage control can be derived as:

$$\begin{cases} \boldsymbol{i}_{2refd} = k_{mmcp}\dfrac{\boldsymbol{u}_{2d}-\boldsymbol{u}_{2refd}}{U_{base}} + k_{mmci}\dfrac{\boldsymbol{x}_{u2d}}{U_{base}} \\ \boldsymbol{i}_{2refq} = k_{mmcp}\dfrac{\boldsymbol{u}_{2q}-\boldsymbol{u}_{2refq}}{U_{base}} + k_{mmci}\dfrac{\boldsymbol{x}_{u2q}}{U_{base}} \\ \dfrac{\mathrm{d}\boldsymbol{x}_{u2d}}{\mathrm{d}t} = -\boldsymbol{N}\boldsymbol{x}_{ugd} + (\boldsymbol{u}_{2d}-\boldsymbol{u}_{2refd}) \\ \dfrac{\mathrm{d}\boldsymbol{x}_{u2q}}{\mathrm{d}t} = -\boldsymbol{N}\boldsymbol{x}_{ugq} + (\boldsymbol{u}_{2q}-\boldsymbol{u}_{2refq}) \end{cases} \tag{11}$$

where $\boldsymbol{x}_{u2d}$ and $\boldsymbol{x}_{u2q}$ are the matrix forms of the integral state variables of the voltage control at *d*- and *q*-axis, respectively; $\boldsymbol{u}_{2refd}$, $\boldsymbol{u}_{2refq}$, $\boldsymbol{i}_{2refd}$, and $\boldsymbol{i}_{2refq}$ are the matrix forms of the voltage and current references at *d*- and *q*-axis, respectively; U_{base} is the voltage base value of the MMC; and k_{mmcp} and

k_{mmci} are the proportional parameter and integral parameter of the proportional and integral (PI) controller in the AC voltage control, respectively.

The inner-current control can be written as:

$$\begin{cases} \boldsymbol{U}_{MMCd}=\left(u_{2d}+\omega\dfrac{L_{arm}}{Z_{base}}\dfrac{\boldsymbol{i}_{2q}}{I_{base}}-k_p\dfrac{\boldsymbol{i}_{2dref}-\boldsymbol{i}_{2d}}{I_{base}}-\dfrac{k_i\boldsymbol{x}_{i2d}}{I_{base}}\right)U_{base} \\ \boldsymbol{U}_{MMCq}=\left(u_{2q}-\omega\dfrac{L_{arm}}{Z_{base}}\dfrac{\boldsymbol{i}_{2d}}{I_{base}}-k_p\dfrac{\boldsymbol{i}_{2qref}-\boldsymbol{i}_{2q}}{I_{base}}-\dfrac{k_i\boldsymbol{x}_{i2q}}{I_{base}}\right)U_{base} \\ \dfrac{\mathrm{d}\boldsymbol{x}_{i2d}}{\mathrm{d}t}=-\boldsymbol{N}\boldsymbol{x}_{i2d}+(\boldsymbol{i}_{2dref}-\boldsymbol{i}_{2d}) \\ \dfrac{\mathrm{d}\boldsymbol{x}_{i2q}}{\mathrm{d}t}=-\boldsymbol{N}\boldsymbol{x}_{i2q}+(\boldsymbol{i}_{2qref}-\boldsymbol{i}_{2q}) \end{cases} \tag{12}$$

where $\boldsymbol{x}_{i2d}$ and $\boldsymbol{x}_{i2q}$ are the matrix forms of the integral state variables of the current control at *d*- and *q*-axis, respectively; I_{base} and Z_{base} are the base values of the current and the impedance, respectively; $\boldsymbol{U}_{MMCd}$ and $\boldsymbol{U}_{MMCq}$ are the matrix forms of the 50 Hz modulation signal at *d*- and *q*-axis, respectively; k_p and k_i are the proportional parameter and integral parameter of the PI controller used in the current control, respectively; and ω is the output angular velocity of the PLL.

3) CCSC

The second harmonic circulating current is suppressed by the CCSC in Supplementary Material A Fig. SA1 and the corresponding HSS model is:

$$\begin{cases} \boldsymbol{U}_{cird}=\left(-2\omega\dfrac{L_{arm}}{Z_{base}}\dfrac{\boldsymbol{i}_{cirq}}{I_{base}}-k_{cirp}\dfrac{\boldsymbol{0}\times\boldsymbol{EI}-\boldsymbol{i}_{cird}}{I_{base}}-k_{ciri}\dfrac{\boldsymbol{x}_{cird}}{I_{base}}\right)U_{base} \\ \boldsymbol{U}_{cirq}=\left(2\omega\dfrac{L_{arm}}{Z_{base}}\dfrac{\boldsymbol{i}_{cird}}{I_{base}}-k_{cirp}\dfrac{\boldsymbol{0}\times\boldsymbol{EI}-\boldsymbol{i}_{cirq}}{I_{base}}-k_{ciri}\dfrac{\boldsymbol{x}_{cirq}}{I_{base}}\right)U_{base} \\ \dfrac{\boldsymbol{x}_{cird}}{\mathrm{d}t}=-\boldsymbol{N}\boldsymbol{x}_{cird}+(\boldsymbol{0}\times\boldsymbol{EI}-\boldsymbol{i}_{cird}) \\ \dfrac{\boldsymbol{x}_{cirq}}{\mathrm{d}t}=-\boldsymbol{N}\boldsymbol{x}_{cirq}+(\boldsymbol{0}\times\boldsymbol{EI}-\boldsymbol{i}_{cirq}) \end{cases} \tag{13}$$

where $\boldsymbol{x}_{cird}$ and $\boldsymbol{x}_{cirq}$ are the matrix forms of the integral state variables of the CCSC control; $\boldsymbol{i}_{cird}$ and $\boldsymbol{i}_{cirq}$ are the matrix forms of the *d*- and *q*-axis components of circulating current, respectivley; $\boldsymbol{U}_{cird}$ and $\boldsymbol{U}_{cirq}$ are the matrix forms of the 100 Hz modulation signals at the *d*- and *q*-axis, respectively; and k_{cirp} and k_{ciri} are the proportional parameter and integral parameter of the PI controller in the CCSC control, respectively.

III. Model Validation and Inrush Current Analysis

Once the HSS model is established, the inrush current I_{rush} can be simulated through the Runge-Kutta algorithm. As the accuracy of the HSS model increases with the truncation order *h*, the value of *h* must be properly selected to balance the modeling accuracy and the computation burden. In this paper, *h* is selected to be 9 according to the criterion developed in [22]. To obtain the maximum inrush current, the closing angle for Y_g-Y and Y_g-D transformers are set to be 30°, and the closing angle for Y-Y_g transformer is set to be 0° [25]. In addition, to investigate the influence of the *V*/*F* controlled MMC, a comparative scenario is considered, where the MMC is replaced by an ideal voltage source with a constant 290 kV voltage output. The results of two scenarios are compared with EMTP simulation results, as shown in Supplementary Material C Figs. SC1 and SC2. The following findings are obtained: ① the simulation results of HSS and EMTP are highly consistent, which demonstrate that the developed HSS model can accurately simulate the phenomenon of inrush current in the WF-MMC-HVDC system; ② the peak values and decay characteristics of the inrush current are quite distinct in two scenarios due to different voltage supplies. Specifically, for Y_g-Y and Y_g-D transformers, the peak values decrease from 5.8 p.u. and 5.6 p.u. to 3.3 p. u. and 3.2 p.u., respectively. For Y-Y_g transformers, the peak value decreases from 3.4 p.u. to 1.9 p.u.; and ③ the Y-Y_g transformer exhibits the minimum peak inrush current. This is because the zero-sequence impedance of the Y-Y_g transformer on the primary side is infinite, which prevents the flow of 3rd and 9th harmonic currents.

Residual flux is one of the crucial factors affecting the characteristics of the inrush current. Here, referring to [26], the residual flux of the three phases is given as 0.6 p.u., –0.3 p.u., and –0.3 p.u., respectively. The corresponding inrush current waveforms are illustrated in Supplementary Material C Figs. SC3 and SC4.

Compared with Figs. SC1 and SC2, the inrush current peaks in Figs. SC3 and SC4 increase significantly, which is expected as the residual flux, generally leading to more severe inrush currents. Besides, we observe that the *V*/*F* controlled MMC leads to a more significant reduction on the inrush current. This phenomenon is investigated in detail using the Y_g-Y transformer. Owing to the frequency domain nature of HSS, waveforms of voltage disturbance Δu_{2A} and current disturbance Δi_{2A} can be accurately decomposed into various harmonics, as shown in Fig. 4, where Δu_{2A} is the phase-*A* disturbance in the PCC voltage of the MMC, and Δi_{2A} is the phase-*A* disturbance in the output current of the MMC, after the occurrence of inrush current. Note that Δi_{2A} is reversed compared with Fig. SC1(a) due to different reference directions.

According to Fig. 4, Δu_{2A} and Δi_{2A} consist of harmonics at the 1st, 3rd, 5th, 7th, and 9th orders, with the 1st harmonic, i.e., 50 Hz component, being dominant. The 3rd and 9th harmonics cannot flow into the MMC through the Y_g-D transformer, hence their amplitudes in Fig. 4(a) are almost zero. Such a result indicates that less severe inrush current is likely to be caused by the voltage drop at 50 Hz.

Based on the main circuit and control diagram of the MMC, an approximate algebraic relationship between Δu_{2A} and Δi_{2A} is established as (14). Please refer to the Supplementary Material D for detail.

$$u_{2A}\approx\frac{\left(\dfrac{1}{2}R_{arm}+k_p\dfrac{U_{base}}{I_{base}}\right)i_{2A}+k_{mmcp}k_pu_{2Aref}+\dfrac{1}{2}L_{arm}\dfrac{\mathrm{d}i_{2A}}{\mathrm{d}t}}{1+k_{mmcp}k_p} \tag{14}$$

When a current disturbance Δi_{2A} emerges due to the inrush current, the voltage disturbance Δu_{2A} can be expressed as:

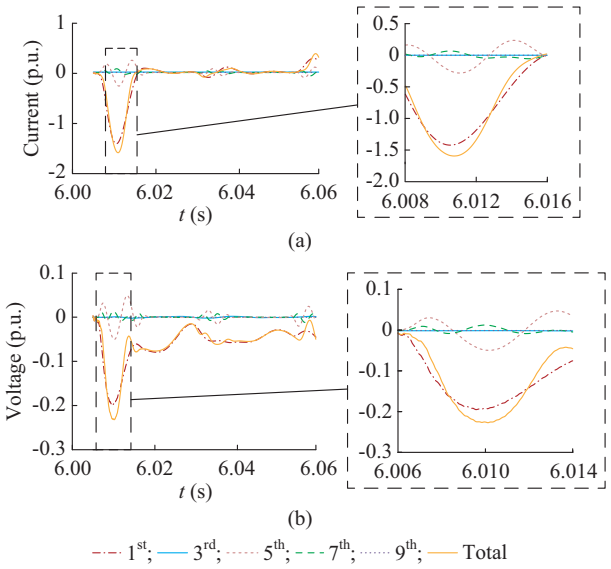

Fig. 4. Harmonic components in Δu_{2A} and Δi_{2A}. (a) Harmonic components in Δi_{2A}. (b) Harmonic components in Δu_{2A}.

$$\Delta u_{2A} \approx \frac{\left(\frac{1}{2}R_{arm}+k_p\frac{U_{base}}{I_{base}}\right)\Delta i_{2A}+\frac{1}{2}L_{arm}\frac{\Delta i_{2A}}{\Delta t}}{1+k_{mmcp}k_p} \tag{15}$$

According to (15), Δi_{2A} is in the same direction as Δu_{2A}, which explains the main cause of the voltage drop during the initial period of the inrush current and the less severe inrush current when compared with the ideal voltage source. Equation (15) also explains the reason why the reduction in the inrush current is more significant when there is a residual flux in the transformer, as a larger inrush current leads to a greater voltage drop.

IV. Influencing Factors

To identify key factors that influence the inrush current in the WF-MMC-HVDC system, the system is partitioned into three subsystems: the WF subsystem, the MMC subsystem, and the transmission line subsystem. The linearized single-input single-output transfer function is obtained from the HSS model to facilitate the analysis from the impedance perspective [27]. Detailed steps are described in Supplementary Material E Fig. SE1.

A. WF Subsystem

1) Impact of Number of Wind Generators

In practical operation, the number of wind generators varies over time, which changes the output power and equivalent impedances of the WF subsystem. The variation of peak values with different numbers of wind generators in operation is provided in Fig. 5. Figure 6 presents the impedance curves with different numbers of wind generators, where Z_{pp} is the positive-sequence impedance, and Z_{nn} is the negative-sequence impedance.

From Fig. 5, it can be observed that the number of wind generators has little impact on the peak value of inrush current.

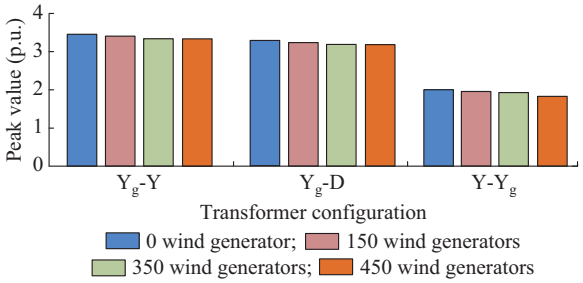

Fig. 5. Variation of peak values with different numbers of wind generators.

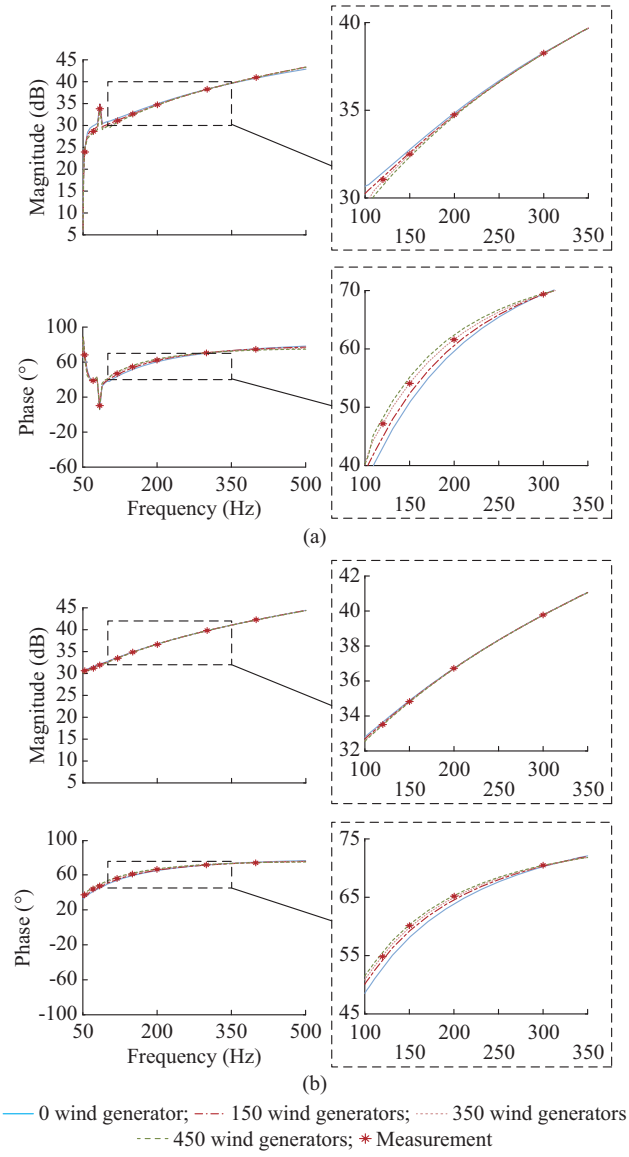

Fig. 6. Impedance curves with different numbers of wind generators. (a) Z_{pp}. (b) Z_{nn}.

The reason can be explained by Fig. 6. The curves of positive- and negative-sequence impedances above the 50 Hz frequency range remain almost constant regardless of the number of wind generators. As a result, WFs have little impact on the inrush current that mainly consists of harmonics with a frequency of 100 Hz and above.

2) Impact of WF Output Power

To analyze the impact of different WF output power on the inrush current, the output power is varied while keeping the number of wind turbines constant. The WF output power is set to be 0 MW, 350 MW, and 700 MW, respectively. The results are shown in Fig. 7.

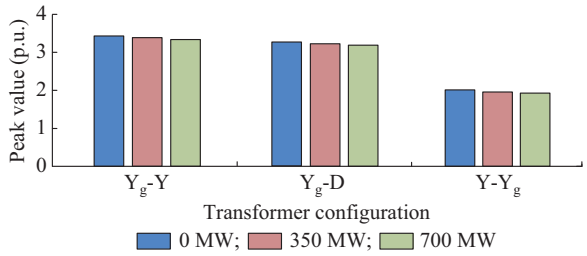

Fig. 7. Peak values of inrush current with different WF output power.

According to Fig. 7, it can be observed that with the increase in WF output power, there is a slight decrease in the peak value of the excitation current (this is due to the increase in transmission power leading to a greater voltage drop along the line), but the overall impact is minimal. Note, the above study does not mean that the impact of offshore WFs on inrush currents can be disregarded in all WF-MMC-HVDC systems. Rather, this effect is case-dependent and strongly influenced by the capacity of the WFs. As the rated capacity increases, the impact of the WF becomes more significant.

B. MMC Subsystem

In addition to *V/F* control, there are other grid-forming control strategies such as droop control and virtual synchronous generator (VSG) control. However, their control bandwidth is relatively small [28], [29], resulting in minimal impact on inrush currents. Therefore, these strategies are not specifically addressed in this paper. According to (15), Δu_2 of the *V/F* control MMC is related to k_{mmcp} and k_p. The impacts of these two parameters on the inrush current are investigated here.

1) Impact of k_{mmcp}

The peak values of the inrush current with different k_{mmcp} are shown in Fig. 8. The corresponding voltage disturbances are compared, as shown in Fig. 9. It is worth noting that, to keep the figure concise, Fig. 9 only displays the dominant 50 Hz and 250 Hz voltage drops as examples.

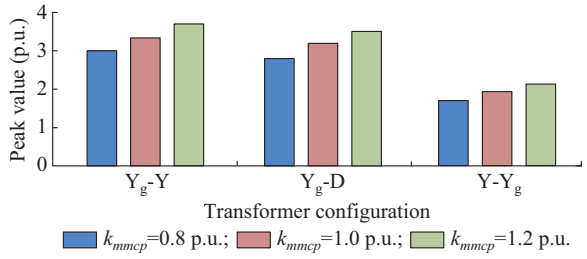

Fig. 8. Peak values of inrush current with different k_{mmcp}.

According to (15), under identical Δi_2, increasing k_{mmcp} contributes to reducing 50 Hz voltage drop in Δu_2. The voltage waveforms shown in Fig. 9 confirm this reasoning. For higher harmonics, as the bandwidth of the AC voltage control loop is usually narrow, changing k_{mmcp} has a relatively small impact. Therefore, the variation in the 250 Hz voltage drop is much smaller than that in the 50 Hz voltage drop, as shown in Fig. 9(b). In short, the larger k_{mmcp} is, the smaller the voltage drop, and consequently, the larger the peak of the inrush current. The data presented in Fig. 8 substantiate the validity of the above analysis.

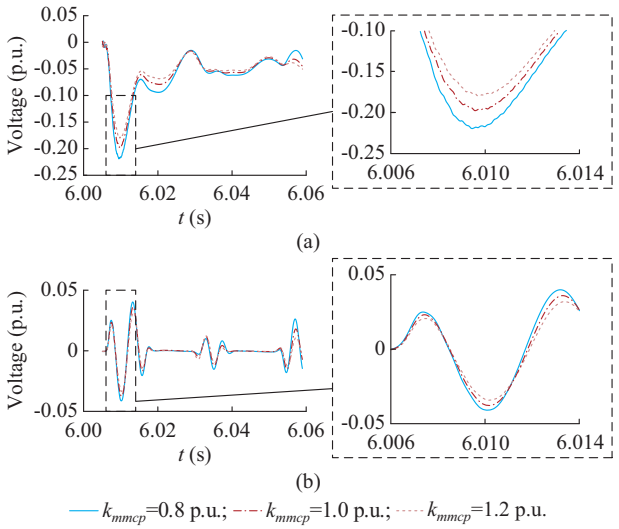

Fig. 9. Harmonics in Δu_2 with different k_{mmcp}. (a) 50 Hz voltage drop. (b) 250 Hz voltage drop.

2) Impact of k_p

Next, the impact of k_p is discussed. The peak values of the inrush current with different k_p are listed in Fig. 10. The corresponding voltage disturbances and the impedance curves of the MMC are investigated, as shown in Figs. 11 and 12, respectively.

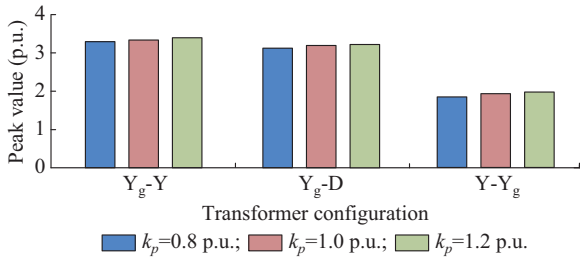

Fig. 10. Peak values of inrush current with different k_p.

Figure 12 indicates that the change of k_p shows a more significant impact on the 250 Hz voltage drop than that of the 50 Hz voltage drop. Due to the wide control bandwidth of the current loop, increasing k_p reduces the impedance magnitude above 100 Hz, which in turn changes the voltage drop at the 250 Hz. On the other hand, the 50 Hz voltage change is not significant as both the numerator and denominator in (15) increase with k_p. Compared with k_{mmcp}, the influence of k_p on Δu_2 and the inrush current is smaller, as shown in Figs. 10 and 11.

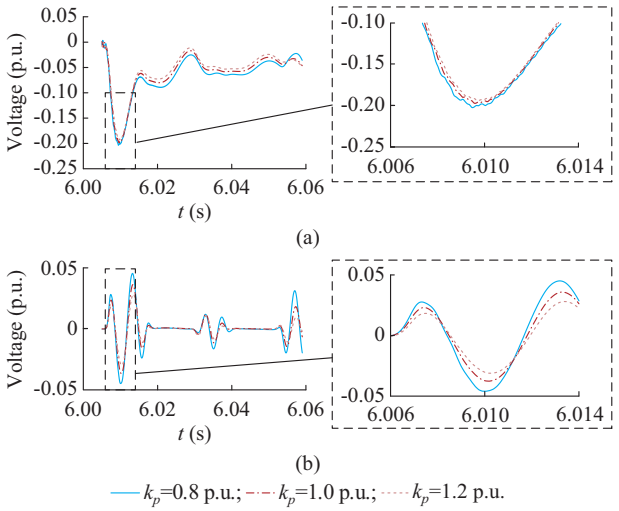

Fig. 11. Harmonics in Δu_2 with different k_p. (a) 50 Hz voltage drop. (b) 250 Hz voltage drop.

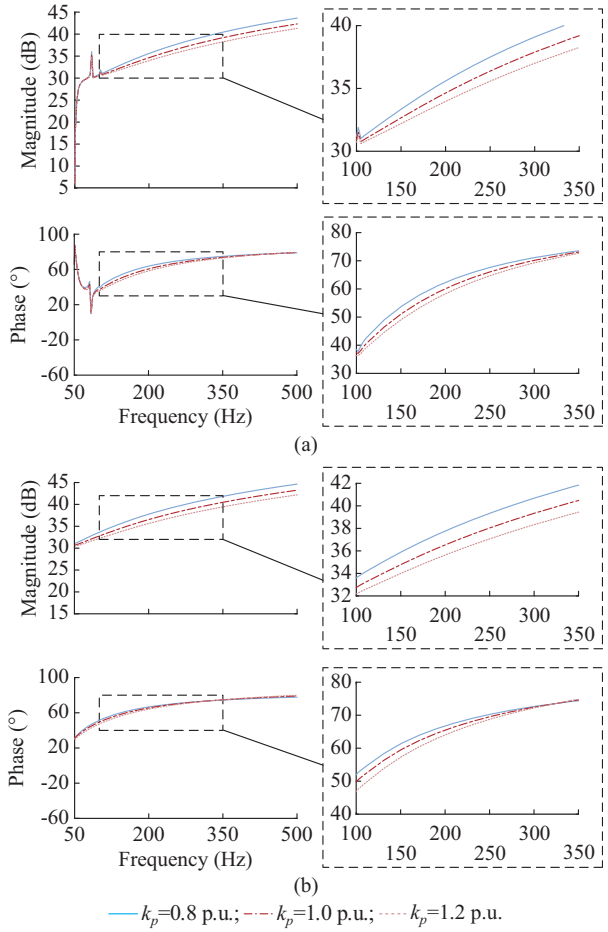

Fig. 12. Impact of k_p on impedance curves. (a) Z_{pp}. (b) Z_{nn}.

C. Transmission Line Subsystem

From the analysis above, it can be concluded that WFs have a small impact on the peak value of the inrush current, whereas the *V/F* control of the MMC alleviates the severity of the inrush current. Therefore, the harmonic issues that occurred in practice are likely to be caused by the transmission lines. Presently, transmission lines in WF-MMC-HVDC systems include two types: overhead lines and submarine cables (mostly used in offshore WFs).

Maintaining the topology of WF-MMC-HVDC system [20], the parameters of an offshore WF-MMC-HVDC system are used, which involves one 47.3 km submarine cable and two 32.2 km submarine cables [4]. The cable parameters are listed in Table IV, and the analysis of inrush current and voltage under different transmission lines is shown in Fig. 13, where proportion indicates the percentage of harmonics relative to the fundamental component.

TABLE IV
CABLE PARAMETERS

Parameter	Cable A	Cable B
Inductance (mH/km)	0.4752	0.4988
Capacitance (μF/km)	0.1269	0.1182
Resistance (Ω/km)	0.0616	0.0698
Length (km)	47.3000	32.2000

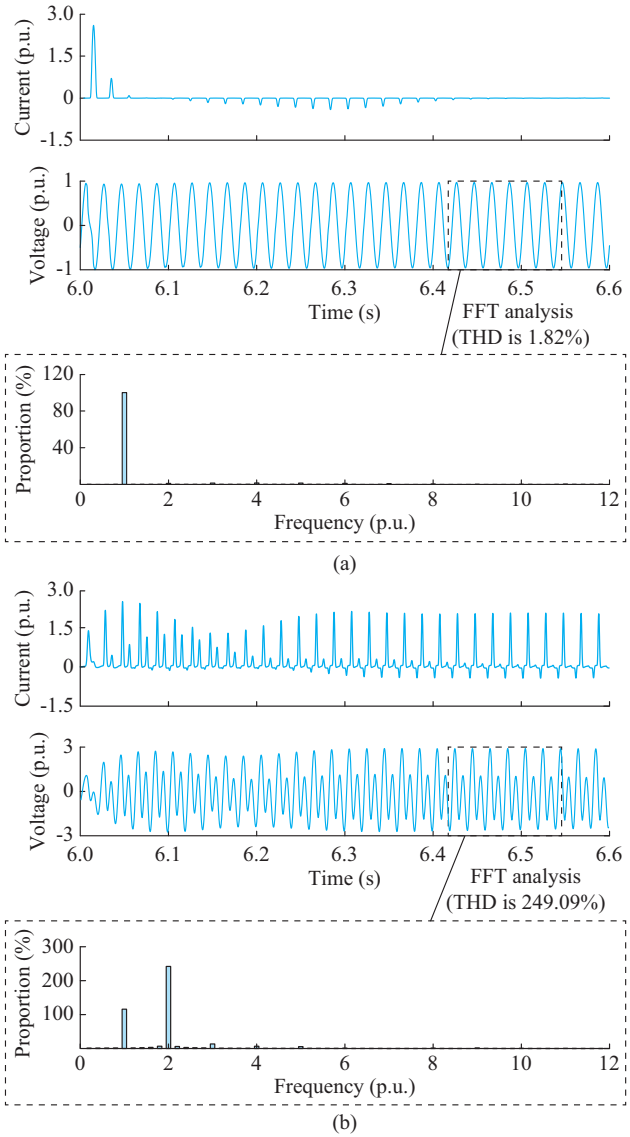

Fig. 13. Analysis of inrush current and voltage under different transmission lines. (a) Overhead line. (b) Cable.

As shown in Fig. 13, cables result in a much more severe inrush current. Harmonics even do not attenuate for a long time, which results in consequences such as tripping of line protection and disconnection of wind generators from the grid.

In Fig. 14, the impedance curves are observed from the 230 kV bus. It is evident that due to the larger capacitance of the cables, a resonance occurs around 100 Hz, significantly amplifying harmonics in the inrush current. In other words, compared with onshore WF systems using overhead lines, offshore WF systems employing cables might encounter more severe inrush current issues. To further demonstrate the impact of submarine cables on inrush current, three cases are designed, as shown in Table V, with cable lengths corresponding to 1 p.u., 0.9 p.u., and 0.8 p.u..

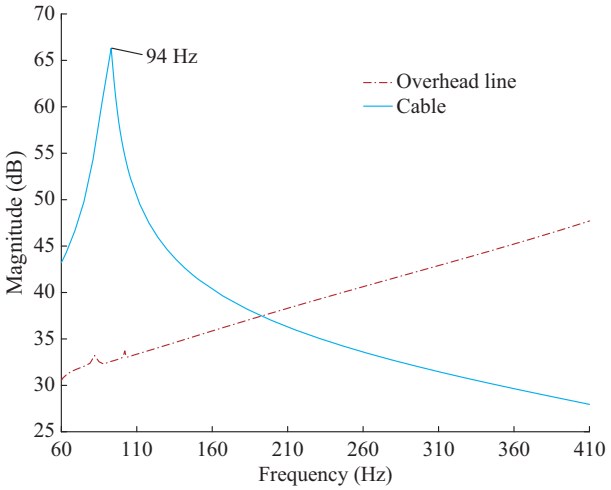

Fig. 14. Impedance curves under different transmission lines.

TABLE V
CASE PARAMETERS

Case	Length of cable A (km)	Length of cable B (km)
1	47.3 × 1.0	32.2 × 1.0
2	47.3 × 0.9	32.2 × 0.9
3	47.3 × 0.8	32.2 × 0.8

In Fig. 15, the impedance curves are presented near 100 Hz for the system under three cases. It is clear that the cable lengths exert a significant impact on resonance. Specifically, case 2 demonstrates the most pronounced resonance effect at 100 Hz, registering a magnitude of 68.7 dB. This is succeeded by case 3, which records a magnitude of 64.7 dB, and case 1, with a magnitude of 59.5 dB.

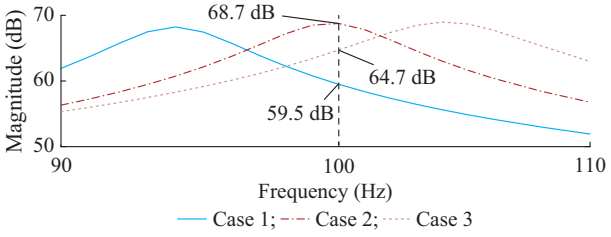

Fig. 15. Impedance curves under different cases.

Figure 16 presents the simulation results of the transformer inrush current and the voltage waveforms at 230 kV bus for case 2 and case 3, and the result of case 1 is shown in Fig. 13(b). The results show that all three cases lead to significant resonant overvoltage. Case 2 exhibits the most severe voltage distortion, with a THD of 286.34%. Case 3 follows with a THD of 264.21%, and case 1 has a THD of 249.09%. These results are consistent with the impedance based resonance analysis in Fig. 15.

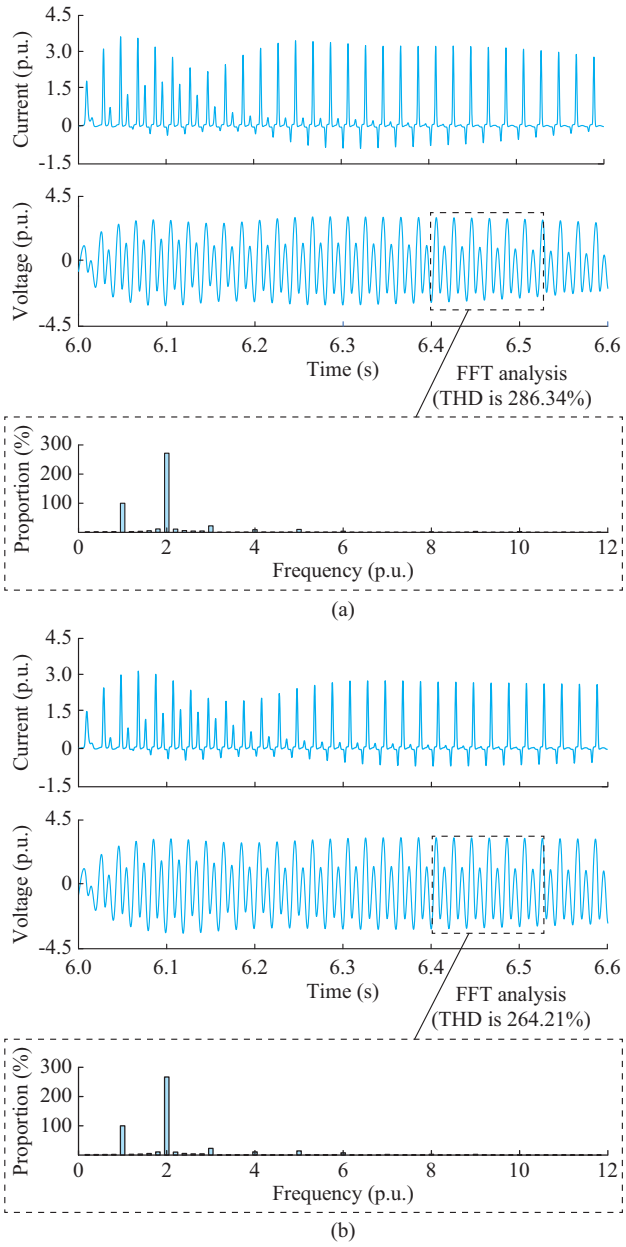

Fig. 16. Simulation results of transformer inrush current and voltage waveforms at 230 kV bus for case 2 and case 3. (a) Case 2. (b) Case 3.

The above cases highlight the significant impact of the cable length on inrush current. Altering the cable length causes a shift in the resonant point of the system, as shown in Fig. 15. When the resonant point aligns with the harmonic frequency range of the inrush current, i.e., the 2nd to 9th harmonics, it amplifies the inrush current, leading to sustained oscil-

lations and resonant overvoltage, as can be observed from the waveforms in Fig. 16.

D. Sensitivity Analysis

To quantify the contribution of various components on the resonance, harmonic resonance modal analysis [30] is applied in this paper. The nodes considered in the analysis include the PCC of the MMC (Node 1), the 230 kV bus (Node 2), and the PCC of the WF (Node 3). The modal impedance of the system in case 1 is depicted in Fig. 17, in which there is a resonance peak at 94 Hz in Node 3, which is consistent with the impedance analysis in Fig. 14.

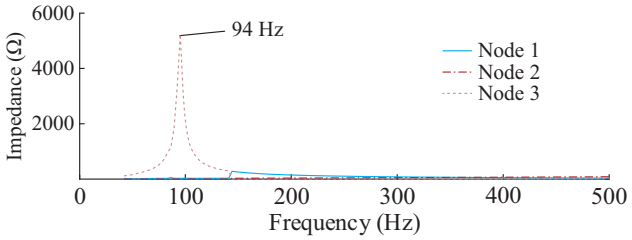

Fig. 17. Modal impedance of system in case 1.

To analyze the primary factors influencing resonance, the following formula is used to calculate parameter sensitivity:

$$\alpha = \frac{(|\lambda_0| - |\lambda_1|)/|\lambda_0|}{(k_0 - k_1)/k_0} = \frac{(1 - |\lambda_1|/|\lambda_0|)}{(1 - k_1/k_0)} \tag{16}$$

where λ is the modal impedance; k is the system parameter; the subscript 0 denotes the value before parameter variation; the subscript 1 denotes the value after parameter variation; and α is the defined modal sensitivity, with a higher value indicating a greater impact of parameter k on the system resonance.

The results of the modal sensitivity analysis are shown in Fig. 18, where L_n ($n = A, B$) is the equivalent inductance of the cables; C_{n1} and C_{n2} are the capacitances of the cables; and T is the impedance of the converter transformer.

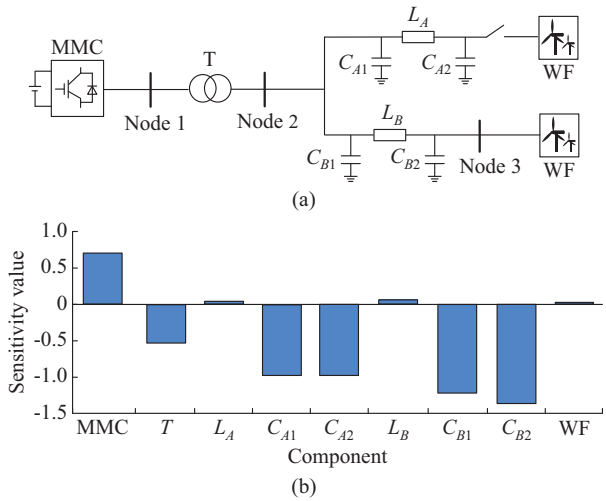

Fig. 18. Sensitivity of critical eigenvalue magnitude with respect to different components. (a) Structure diagram of offshore WF-MMC-HVDC system. (b) Results of modal sensitivity analysis.

The result indicates that the sensitivity values of C_{n1} and C_{n2} are the highest, followed by the impedances of the MMC and the converter transformer. This indicates that the capacitances of cables are the main cause of the resonance around 94 Hz, while the impacts of the WFs and line inductances are limited.

V. Conclusion

This paper develops an HSS model of WF-MCC systems with a saturable transformer to investigate the characteristics of the transformer inrush current in WF-MMC-HVDC systems. The main conclusions can be summarized as follows:

1) For three commonly-used winding connections, i.e., Y_g-Y, Y_g-D, and Y-Y_g, the former two exhibit a higher peak of inrush currents, whereas the peak value for Y-Y_g is relatively smaller due to its infinite zero-sequence impedance on the primary side, which suppresses the 3rd and 9th harmonics. Therefore, more attentions should be given when Y_g-Y and Y_g-D transformers are energized.

2) The influence of WFs is small, whereas the *V*/*F* controlled MMC would attenuate the peak value of the inrush current due to the 50 Hz voltage drop caused by the inrush current. Compared with current loops, the proportional term of the *V*/*F* control loop has the most significant impact on the inrush current.

3) The severity of inrush current is closely related to transmission lines, whose parameters may vary in a wide range. By using the parameters of a real-world offshore WF-MMC-HVDC system, it is found that the large capacitance of the offshore cable leads to a decrease in the natural resonance frequency, which may significantly amplify the harmonics in inrush currents.

References

[1] J. Wang, W. Chen, Y. Liu *et al.*, "High-frequency resonance analysis and impedance reshaping control of MMC-HVDC system based on frequency coupling impedance model," *Journal of Modern Power Systems and Clean Energy*, vol. 12, no. 2, pp. 646-657, Mar. 2024.

[2] J. Li, X. Xie, J. Yang *et al.*, "Analysis and suppression of subsynchronous oscillation of Rudong wind power through MMC-HVDC system," in *Proceedings of 2021 Annual Meeting of CSEE Study Committee of HVDC and Power Electronics*, Xi'an, China, Dec. 2021, pp. 151-158.

[3] G. Li, H. Ye, and Z. Bin, "High-frequency oscillation mechanism analysis of wind farm-side MMC station considering converter transformer stray capacitance," *International Journal of Electrical Power & Energy Systems*, vol. 153, p. 109179, Nov. 2023.

[4] D. Yang, R. Song, Z. Xiang *et al.*, "Causes and suppression measures of resonance overvoltage in offshore wind power AC transmission system," *Automation of Electric Power Systems*, vol. 46, no. 15, pp. 171-177, Aug. 2022.

[5] S. Wu, Y. Ren, Y. Wang *et al.*, "Residual flux measurement of power transformer based on transient current difference," *IEEE Transactions on Magnetics*, vol. 58, no. 2, pp. 1-5, Feb. 2022.

[6] C. Huo, Y. Wang, S. Wu *et al.*, "Research on residual flux density measurement for single-phase transformer core based on energy changes," *IEEE Transactions on Instrumentation and Measurement*, vol. 70, pp. 1-9, Nov. 2021.

[7] Z. Chen, H. Li, X. Dong *et al.*, "Magnetizing inrush current elimination strategy based on a parallel type asynchronous closing hybrid transformer," *IEEE Transactions on Power Electronics*, vol. 38, no. 1, pp. 931-943, Jan. 2023.

[8] M. Lu, "An inrush current limiting strategy for virtual-oscillator-controlled grid-forming inverters," *IEEE Transactions on Energy Conversion*, vol. 38, no. 3, pp. 1501-1510, Sept. 2023.

[9] A. Ramirez, "Frequency-domain computation of steady and dynamic

states including nonlinear elements," *IEEE Transactions on Power Delivery*, vol. 24, no. 3, pp. 1609-1615, Jul. 2009.
[10] S. Sanders, J. Noworolski, X. Liu *et al*., "Generalized averaging method for power conversion circuits," *IEEE Transactions on Power Electronics*, vol. 6, no. 2, pp. 251-259, Apr. 1991.
[11] Q. Zhong, Y. Qiu, Y. Zhao *et al*., "Interharmonic analysis model of photovoltaic grid-connected system with extended dynamic phasors," *Journal of Modern Power Systems and Clean Energy*, vol. 9, no. 6, pp. 1540-1547, Nov. 2021.
[12] P. Chen, P. Zhao, L. Lu *et al*., "Dynamic phasor-based stochastic transient simulation method for MTDC distribution system," *IEEE Transactions on Industrial Electronics*, vol. 70, no. 11, pp. 11516-11526, Nov. 2023.
[13] X. Guo, Z. Lu, B. Wang *et al*., "Dynamic phasors-based modeling and stability analysis of droop-controlled inverters for microgrid applications," *IEEE Transactions on Smart Grid*, vol. 5, no. 6, pp. 2980-2987, Nov. 2014.
[14] J. J. Chavez and A. Ramirez, "Dynamic harmonic domain modeling of transients in three-phase transmission lines," *IEEE Transactions on Power Delivery*, vol. 23, no. 4, pp. 2294-2301, Oct. 2008.
[15] P. De Rua, Ö. C. Sakinci, and J. Beerten, "Comparative study of dynamic phasor and harmonic state-space modeling for small-signal stability analysis," *Electric Power Systems Research*, vol. 189, pp. 1-5, Dec. 2020.
[16] P. D. Achlerkar and B. K. Panigrahi, "Dynamic harmonic domain modeling and stability augmented design of inverter interface to weak and unbalanced grid," *IEEE Transactions on Power Delivery*, vol. 37, no. 4, pp. 3097-3110, Aug. 2022.
[17] K. Gao, R. Xie, and G. Zhang, "Harmonic analysis of nonlinear periodic network using the dynamic harmonic domain," in *Proceedings of 2020 7th International Forum on Electrical Engineering and Automation*, Hangzhou, China, Sept. 2020, pp. 616-622.
[18] E. Karami, G. B. Gharehpetian, and M. Madrigal, "A step forward in application of dynamic harmonic domain: phase shifting property of harmonics," *IEEE Transactions on Power Delivery*, vol. 32, no. 1, pp. 219-225, Feb. 2017.
[19] E. Karami, M. Madrigal, G. B. Gharehpetian *et al*., "Single-phase modeling approach in dynamic harmonic domain," *IEEE Transactions on Power Systems*, vol. 33, no. 1, pp. 257-267, Jan. 2018.
[20] K. Ji, H. Pang, S. Liu *et al*., "Impedance analysis considering unstable subsystem poles for MMC-HVDC-based wind farm integration system," *CSEE Journal of Power and Energy Systems*, vol. 8, no. 2, pp. 634-639, Mar. 2022.
[21] P. Kundur, *Power System Stability and Control*. New York: McGraw-Hill, 1994.
[22] M. T. Aung and J. V. Milanovic, "The influence of transformer winding connections on the propagation of voltage sags," *IEEE Transactions on Power Delivery*, vol. 21, no. 1, pp. 262-269, Jan. 2006.
[23] A. M. Kettner, L. R. Chamorro, J. K. M. Becker *et al*., "Harmonic power-flow study of polyphase grids with converter-interfaced distributed energy resources – part I: modeling framework and algorithm," *IEEE Transactions on Smart Grid*, vol. 13, no. 1, pp. 458-469, Jan. 2022.
[24] H. Yang and S. Dieckerhoff, "Truncation order selection method for LTP-theory-based stability analysis of converter dominated power systems," *IEEE Transactions on Power Electronics*, vol. 36, no. 11, pp. 12168-12172, Nov. 2021.
[25] Y. Yu, Z. Zhang, W. He *et al*., "Simulation analysis of inrush current and electromagnetic-force characteristics of converter transformer during no-load closing," in *Proceedings of 2023 2nd International Conference on Power Systems and Electrical Technology*, Milan, Italy, Aug. 2023, pp. 137-143.
[26] N. Chiesa, B. A. Mork, and H. K. Høidalen, "Transformer model for inrush current calculations: simulations, measurements and sensitivity analysis," *IEEE Transactions on Power Delivery*, vol. 25, no. 4, pp. 2599-2608, Oct. 2010.
[27] C. Zhang, M. Molinas, S. Føyen *et al*., "Harmonic-domain SISO equivalent impedance modeling and stability analysis of a single-phase grid-connected VSC," *IEEE Transactions on Power Electronics*, vol. 35, no. 9, pp. 9770-9783, Sept. 2020.
[28] M. A. Elshenawy, A. Radwan, and Y. A. R. I. Mohamed, "Unified sequence impedance models of synchronous generator-and virtual oscillator-based grid-forming converters," *IEEE Transactions on Power Delivery*, vol. 39, no. 1, pp. 56-70, Feb. 2024.
[29] X. Meng, J. Liu, and Z. Liu, "A generalized droop control for grid-supporting inverter based on comparison between traditional droop control and virtual synchronous generator control," *IEEE Transactions on Power Electronics*, vol. 34, no. 6, pp. 5416-5438, Jun. 2019.
[30] F. Zhong, S. Xie, Y. Peng *et al*., "Harmonic resonance analysis and suppression for suburban railway continuous power supply systems," *Journal of Modern Power Systems and Clean Energy*, vol. 13, no. 1, pp. 253-264, Jan. 2025.

Hanwen Wang received the M.S. degree from Sichuan University, Sichuan, China, in 2022. He is currently pursuing the Ph.D. degree at the School of Electrical Engineering, Sichuan University. His research interests include modeling and harmonic analysis of flexible DC transmission system.

Yang Wang received the B.S. degree in electrical engineering from Zhejiang University, Hangzhou, China, in 2012, and the Ph.D. degree in electrical and computer engineering from the University of Alberta, Edmonton, Canada, in 2017. He is currently a Research Fellow with the College of Electrical Engineering, Sichuan University, Chengdu, China. His main research interests include power quality and integration of renewable energy.

Xianyong Xiao received the Ph.D. degree from Sichuan University, Chengdu, China, in 2010. He is currently a Professor and the Dean with the College of Electrical Engineering and Information Technology, Sichuan University. His research interests include power quality and its control, distribution system reliability, and green friendly smart grid.

Zhiquan Ma received the M.S. degree from Huazhong University of Science and Technology, Wuhan, China, in 2006. He is currently working as a Senior Engineer in State Grid Zhejiang Electric Power Research Institute, Hangzhou, China. His research interests include power quality measurement and analysis.

Qunwei Xu received B.S. degree from Wuhan University, Wuhan, China, in 2012, and the Ph.D. degree from Zhejiang University, Hangzhou, China, in 2017. Currently, he works at the State Grid Zhejiang Electric Power Research Institute, Hangzhou, China. His research interests include monitoring, analysis, and active control improvement of power quality in new power system.